MATOME MOTHETHA[1, 2], KEFENI KEBEDE[3],
VHAHANGWELE MASINDI[1, 4], TITUS MSAGATI[3]

# EMPLOYMENT OF Ca²⁺-RICH MgO NANOPARTICLES FOR EFFECTIVE TREATMENT OF REAL ACID MINE DRAINAGE

The efficacy of $Ca^{2+}$-rich MgO nanoparticles for the effective treatment of real acid mine drainage (AMD) was evaluated. The optimized parameters include the feedstock dosage and contact time. The experimental results were underpinned using state-of-the-art analytical techniques and instruments such as FTIR, HR-FIB/SEM, EDS, XRF, and XRD. The pH REDOX equilibrium (in C language) (PHREEQC) model was also employed to complement experimental results. Optimum conditions were observed to be 45–60 min of mixing time, $\geq$10 000 mg/dm³ of feedstock dosage, i.e., $Ca^{2+}$-rich MgO nanoparticles, and ambient temperature and pH. The metal content ($Fe^{3+}$, $Mn^{2+}$, $Cr^{2+}$, $Cu^{2+}$, $Ni^{2+}$, $Pb^{2+}$, $Al^{3+}$, and $Zn^{2+}$) embedded in AMD matrices was practically removed ($\geq$99% removal efficacies) whilst the sulfate was also attenuated humongous ($\geq$40%). The PHREEQC predicted metals to exist as multi-valent including carbonates and other chemical complexes. Chemical species in real AMD were predicted to precipitate as metals hydroxides, (oxy)-hydroxides, carbonates, and (oxy)-hydro-sulfates. Henceforth, the use of $Ca^{2+}$-rich MgO nanoparticles was proved to be effective in the treatment of AMD from coal mining activities. However, a polishing technology will be required to further remove residual sulfates. This could be pursued to recover sulfate in valuable form and then reclaim drinking water for domestic purposes or other defined uses (end-use). This will then be the most effective closed-loop approach in the management of AMD under the circular economy (CE) concept.

---

[1]Department of Environmental Sciences, College of Agriculture and Environmental Sciences, University of South Africa (UNISA), P.O. Box 392, Florida, 1710, South Africa.

[2]Research and Committees Unit, Legislature Department, City of Ekurhuleni, Private Bag X1069, Germiston 1400, South Africa.

[3]Institute of Nanotechnology and Water Sustainability, College of Science, Engineering and Technology, University of South Africa, Private Bag X6, Florida 1710, South Africa, corresponding author T. Msagati, email address: msagatam@unisa.ac.za

[4]Magalies Water, Scientific Services, Research and Development Division, Erf 3475, Stoffberg Street, Brits 0250, South Africa.

## 1. INTRODUCTION

Contamination of different receiving environments by acid mine drainage (AMD) has been a topical issue of prime concern in minerals-rich countries. This is mainly attributed to the magnitude of environmental impacts embodied in the chemical species embedded in acid mine drainage [1, 2]. Acid mine drainage is rich in toxic and hazardous chemical species such as $Al^{3+}$, $Fe^{3+}$, $Mn^{2+}$, heavy metals ($Cu^{2+}$, $Zn^{2+}$, $Ni^{2+}$, $Pb^{2+}$), radionuclides (U), oxyanions (sulfates), metalloids ($As^{3-}$ and $Cr^{2+}$), and acidity ($H^+$). In addition, this metalliferous drainage is rich in total dissolved solids (TDS) and high electrical conductivity ($EC$) [3–5]. The chemical properties of AMD are a result of the hydro-geo-chemical properties of the surrounding areas. In most instances, pyrite ($FeS_2$), arsenopyrite (FeAsS), and other sulfide-bearing minerals (ZnS, PbS, and CuS, etc.) in the void that has been left after the extraction of coal and gold get exposed to oxidising conditions, i.e., water and oxygen. This led to the formation of sulfate-rich drainage that is very acidic. The acidity accelerates the leaching of different chemical components from the surrounding geology hence further enriching mine water with toxic and hazardous chemical species [3–5]. On intentional or passive discharge, these chemicals have the potential to pose threats and ecological stresses to the receiving environment and living organisms on exposure. According to eco-toxicological studies and epidemiological reports, chemicals in AMD can pose carcinogenic, mutagenic, and teratogenic effects to living organisms on exposure. This will also degrade the suitability of the given environment to foster life. A recent case in South Africa led to the death of dozen fish species in the river due to exposure to the chemicals on a passively discharged AMD from abandoned and derelict coal mines [6, 7]. As such, the metalliferous mine drainage needs to be treated before the contamination of the environment [8].

Various technologies that rely on different mechanisms have been developed, piloted, and implemented [9] and they include precipitation, filtration, ion exchange, adsorption, distillation, crystallization, bio-remediation, and phytoremediation, amongst others [1, 5]. Some techniques employ either hybrid or combined mechanisms in a sequential or synergistic manner [2]. These mechanisms have advantages and disadvantages with adsorption having the challenges of limited adsorption capacity, quick saturation, and selective ability. Moreover, the regenerant from the adsorbent poses secondary pollution and this poses challenges with the disposal of the adsorbent unless if valorisation is explored [10]. Membrane filtration has high efficacy but at the expense of the environment since it produces brine and consumes energy. Ion exchange is promising but the regenerants and secondary pollution have been a main issue of concern whilst bio-(phyto)-remediation requires a large space of land and it has challenges with concentrated solutions [11, 12]. Amid the challenges of these other techniques, precipitation has been recommended as the best technique for AMD treatment primarily due to its efficacy in concentrated solutions with very small dosages. Its flexibility in terms of selec-

tive metals recovery further gained more attention in water treatment [12, 13]. Specifically, different alkaline generating agents have been used for acid mine drainage treatment and they include lime, periclase, brucite, hydrated lime, limestone, dolomite, soda ash, caustic soda, magnesium bi-carbonates, and tailings [13]. However, some agents have drawbacks that limit their application, with Ca-based minerals having a challenge of producing highly mineralised and toxic sludge while Na-based produce highly mineralised sludge and sulfate is kept in solutions as sodium sulfate complex [12, 14]. Periclase ($MgO$) and brucite ($Mg(OH)_2$) nanoparticles (NPs) have been employed for the treatment of real acid mine drainage with the advantage of the sequential recovery of minerals from mine water and this was proved to be efficient and effective [15, 16]. However, the $Ca^{2+}$-rich MgO NPs have never been used for the treatment of AMD and this will have the advantage of removing metals and sulfate altogether. To the best of our knowledge, this is the first study in design and execution to explore the application of $Ca^{2+}$-rich MgO NPs for the treatment of AMD from coal mining and then point out the mechanism that underpins the effective removal of inorganic contaminants.

## 2. MATERIALS AND METHODS

*Samples collection*. Real AMD was collected from a coal mine in Mpumalanga province, South Africa. The effluent was seeping through the toe of a coal stockpile. This AMD is concentrated and fully oxidised due to evaporation and exposure to atmospheric oxygen, hence Fe(III) will exist in an elevated concentration. The wide--mouth high-density polyethylene (HDPE) bottles were used for sample collection, while the suspended solids and debris were removed by filtration using Macherey–Nagel filter papers (MN 615, 125 mm). After collection, samples were stored in a cooled bag and transferred to the laboratory. $Ca^{2+}$-rich MgO NP was procured from Sterkfontein carbonates. The samples were dry when received and they were in the particle size range not exceeding 32 nm. The samples were used as received from the Sterkfontein carbonates (supplier).

*Treatment of real AMD. Optimisation studies.* The batch experimental approach was used for the treatment of AMD using the $Ca^{2+}$-rich MgO NPs. Graded volumetric flasks loaded with 1000 cm³ of AMD were used. The mixtures were mixed at 250 rpm for a specified interval and dosages. The overhead stirrers mounted on a Philip and Bird stirrer equipped with six propellers were utilised. The contact time amounted to 5, 10, 15, 30, 45, and 60 min whilst the dosages of $Ca^{2+}$-rich MgO NP were equal to 500, 1000, 2500, 5000, 10 000 and 15 000 mg/dm³. The results were presented as mean values of experiments performed in triplicate. The optimum contact time was first identified and

then used to identify the optimum $Ca^{2+}$-rich MgO NPs dosage. $Ca^{2+}$-rich MgO NPs samples were weighted using an analytical balance, with the precision restricted to two decimal places.

The percentage removal efficiency ($RE$) of the contaminants in AMD after the treatment, was estimated using the equation

$$RE = \frac{C_0 - C_e}{C_0} \times 100\% \tag{1}$$

where $C_0$ is the initial concentration of the contaminant and $C_e$ is its final concentration.

*Sample characterisation.* For the characterisation of the in-situ properties, i.e., pH, electrical conductivity ($EC$) and total dissolved solids (TDS) of AMD, a multi-parameter probe (HANNA instrument, HI9828) was used. Ions contained in the raw and treated AMD ($Fe^{3+}$, $Mn^{2+}$, $Cr^{2+}$, $Cu^{2+}$, $Ni^{2+}$, $Pb^{2+}$, $Al^{3+}$, $Zn^{2+}$, $SO_4^{2-}$, $Ca^{2+}$, and $Mg^{2+}$) were determined by inductively coupled plasma-optical emission spectrometry (ICP-OES) (Agilent Technologies 5110, coupled with Agilent SPS 4 autosampler) and the inductively coupled plasma mass spectrometry (ICP-MS) (Thermo Scientific's XSERIES 2, coupled with ASX-520 autosampler). Thermo Fisher Scientific's gallery plus discrete analyser photo spectrometer was used for base metals analyses, including sulfates. National Institute of Standards and Technology (NIST) standards reference materials and quality control procedures were duly considered during the experiments and analyses.

To study the mineralogical characteristics of the $Ca^{2+}$-rich MgO NPs, and resultant sludge, X-ray diffraction (XRD) (Panalytical's X'Pert PRO X-ray diffractometer along with Philips PW 1710 diffractometer with graphite secondary monochromatic source was used. Their elemental compositions were determined using X-ray fluorescence (XRF) (Thermo Scientific's ARL PERFORM'X Sequential X sequential XRF spectrometer coupled with the UniQuant software for standardless quantitative analysis). Functional groups were identified using Fourier transform infrared spectroscopy (FTIR) with the use of Perkin-Elmer Spectrum 100 FTIR spectrometer coupled with Perkin-Elmer's universal attenuated total reflectance (ATR) sampling accessory with a diamond crystal. To complement the XRD and XRF results, the morphological, mapping properties, and elemental properties were determined using high resolution (HR) field emission scanning electron microscope (FE-SEM) (SmartSEM®-Auriga®) coupled with focused ion Beam (FIB) and energy dispersive X-ray spectroscopy (EDS). EDS/SEM and FIB/SEM enable precise and highly accurate measurements, while detailed and high-resolution and practically undistorted images can be also obtained.

*Complementary experimental results with a geochemical model.* To complement the experimental results and determine the aqueous species and mineral phases more

likely synthesized from the interaction of the nanocomposite and real AMD, geochemical modelling was applied. To determine the speciation and calculate the saturation indexes (*SIs*) of the mineral phases based on compositions of raw water and feedstock minerals, a pH REdox EQuilibrium (in C language) (PHREEQC) geochemical model with the use of the WATEQ4F, PHREEQC and MINTEQ database were employed [14].

## 3. RESULTS AND DISCUSSION

### 3.1. OPTIMISATION STUDIES

The *EC*, pH, $Ca^{2+}$, and $Mg^{2+}$ levels (Fig. 1a) and the percentage removal of inorganic contaminants in the function of $Ca^{2+}$-rich MgO NPs dosage are shown in Fig. 1.
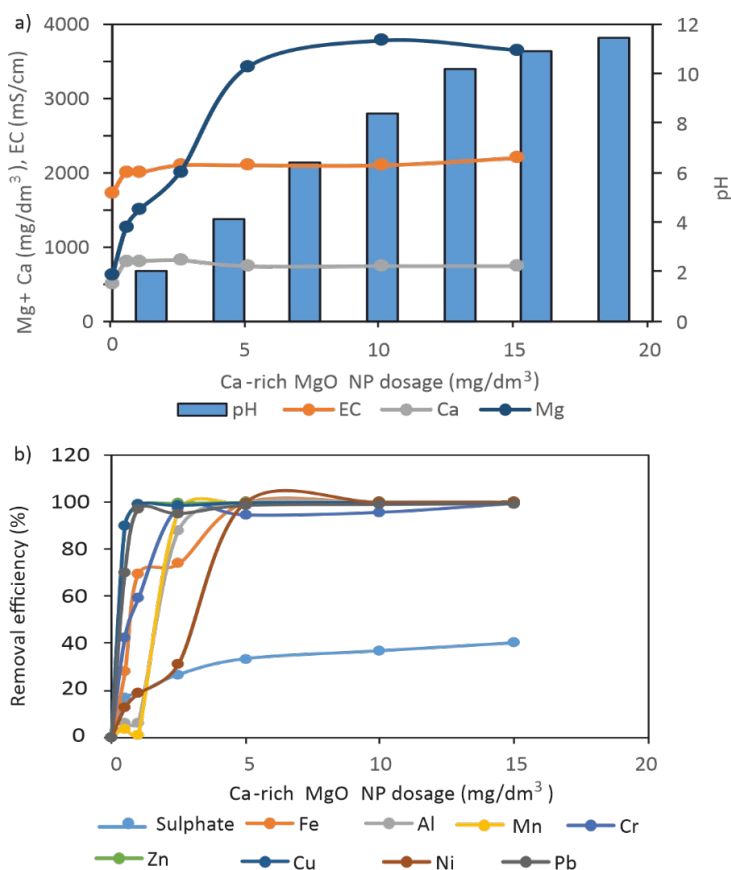


Fig. 1. $Mg^{2+}$ and $Ca^{2+}$ concentration, *EC* (mS/cm), pH (a), and the removal efficiencies of inorganic contaminants (b) in the function of $Ca^{2+}$-rich MgO NPs dosage; contact time 45 min, mixing speed 250 rpm, room temperature

Ca$^{2+}$-rich MgO NPs was observed to influence the levels of Ca$^{2+}$, Mg$^{2+}$, *EC*, and pH of the treated AMD. As expected (Fig. 1a), pH and Mg$^{2+}$ levels increased with an increase in the NPs dosage. Similarly, there was a rapid increase in both *EC* value and Ca$^{2+}$ concentration when the lowest dosage of NPs was applied (0.5 g/dm$^3$) thereafter, their levels were observed to be significantly the same throughout varying NPs dosages. This denotes that there is the removal of dissolved substances that contributes to an increase in dissolved solids and electrical conductivity. A plateau of Ca$^{2+}$ concentration may be linked to the formation of gypsum with the removal of sulfate. As the pH was increasing, the Mg$^{2+}$ concentration was observed to decrease at the dose of 15 g/dm$^3$ and this could be attributed to the precipitation of Mg$^{2+}$ as brucite [1]. The Mg$^{2+}$ concentration was observed to increase from 622 to 3766 mg/dm$^3$ in 45 min at 10 g/dm$^3$ of the Ca$^{2+}$-rich MgO NPs dosage (sixfold increase). An increase in Mg$^{2+}$ concentration shows the dissolution of Ca$^{2+}$-rich MgO NPs but this was expected since the Mg-based material was applied. In particular, pH increased from 2 to 11.42 at a Ca$^{2+}$-rich MgO NPs dosage of 15 g/dm$^3$. PHREEQC geochemical model also predicted Ca$^{2+}$ and Mg$^{2+}$ to exist as divalent species in an aqueous solution. Moreover, the model also predicted these base cations to exist as different complexes in an aqueous solution and these include sulfate and hydroxide complexes. Furthermore, the model predicted Ca$^{2+}$ to be removed as gypsum and Mg$^{2+}$ precipitated as brucite (Mg(OH)$_2$). Findings from this section are consistent with those reported in the literature [1, 17].

As shown in Fig. 1b, there was an increase in the *RE* of inorganic contaminants with an increase in the Ca$^{2+}$-rich MgO NPs dosages. The increase in dosage proportionally led to an increase in alkalinity due to the addition of Ca$^{2+}$ and Mg$^{2+}$ ions. Within the lowest dosage of Ca$^{2+}$-rich MgO NPs (0.5 g/dm$^3$), the analyzed metal ions were observed to have been removed significantly (≥95%) due to precipitation insoluble species [18, 19]. The removal of sulfate also gradually increased when Ca$^{2+}$-rich MgO NPs dosage increased from 1 to 15 g/dm$^3$, with a maximum *RE* of 38%. This could be attributed to the formation of gypsum when reacting with AMD rich in sulfate. In the dosage range of Ca$^{2+}$-rich MgO NPs from 5 to 15 g/dm$^3$, no significant changes in metals removal were observed, except for sulfate which was gradually increasing, hence 10 g/dm$^3$ was taken as the optimum dosage for the removal of metals from AMD. Poor *RE* of sulfate could be attributed to the lack of enough Ca$^{2+}$ in the matrices of the Ca$^{2+}$-rich MgO NPs, significantly supporting the removal of sulfate as gypsum. PHREEQC predicted the removal of minerals in the form of metals hydroxides, oxy-(hydro)-sulfates, and gypsum, amongst others. This could explain an insignificant increase in Ca$^{2+}$ concentration with an increase in Ca$^{2+}$-rich MgO NPs dosage.

As shown in Fig. 2a, there was a proportional increase and fluctuation of *EC* and Ca$^{2+}$ levels with an increase in contact time. This could denote some stoichiometrical relation during the interaction of AMD and Ca-rich MgO NPs. For contact time from 0 to 5 min, there was an uptrend of Ca$^{2+}$ concentration, i.e., it increased from 495 to 814 mg/dm$^3$

(64% increase), and the *EC* level increased from 1709 to 2200 mS/cm (28% increase), thereafter, these parameters were observed to gradually decrease with contact time. Their decrease may be attributed to the interaction of $Ca^{2+}$ and sulfate leading to the formation of gypsum.
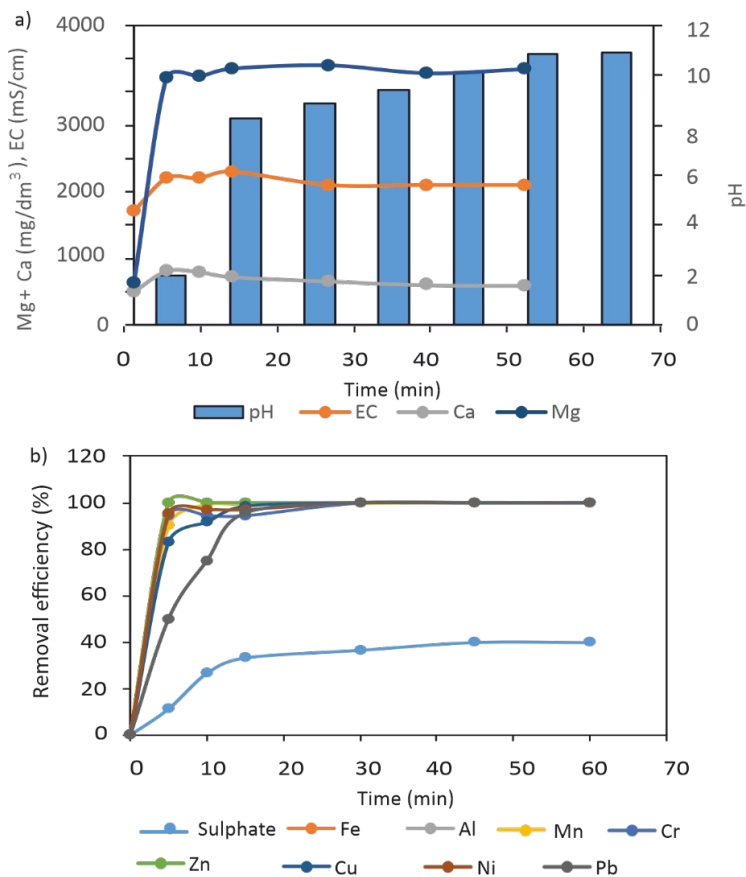


Fig. 2. Time dependences of $Mg^{2+}$ and $Ca^{2+}$ concentrations, *EC*, pH (a),
and the removal efficiencies of inorganic contaminants (b);
$Ca^{2+}$-rich MgO NPs dosage 10 g/dm³, 250 rpm mixing speed, room temperature

Similar results were predicted by PHREEQC geochemical modelling. Furthermore, the reduction of *EC* further denotes the attenuation of dissolved substances from AMD. On the other hand, the $Mg^{2+}$ concentration was observed to increase with an increase in contact time (from 622 to 3710 mg/dm³ (a sixfold increase in 5 min). Thereafter, there was no significant reduction in $Mg^{2+}$ content which was observed as the contact time was increasing which denotes that the reaction of $Ca^{2+}$-rich MgO NPs with contaminants precedes very fast. pH was also observed to increase from 2 to 10.93 after 60 min. The

$Ca^{2+}$-rich MgO NPs dosage of 10 g/dm$^3$ was taken as the optimum dosage to effectively remove the metals and increase the pH to the desired limit. An increase in $Mg^{2+}$ concentration implies an increase in alkalinity to enable the precipitation of insoluble hydroxides, oxy-(hydro)-sulfates, and carbonates including sulfate as gypsum.

As expected, there was an increase in the removal of inorganic contaminants with an increase in contact time (Fig. 2b). The removal efficacies were observed to be rapid for contact time from 0 to 30 min, thereafter, no significant change was observed during the interaction of AMD and $Ca^{2+}$-rich MgO NPs. As such, 45 min seemed to be sufficient for the treatment of AMD with $Ca^{2+}$-rich MgO NPs. Specifically, there were ≥99.5% removal for $Fe^{3+}$, $Al^{3+}$, $Mn^{2+}$, $Cr^{2+}$, $Zn^{2+}$, $Cu^{2+}$, $Ni^{2+}$, and $Pb^{2+}$ except for sulfate that reached ≥40% *RE*. There is a direct proportion between the $Ca^{2+}$ content trend and sulfate concentration precipitation to form gypsum. A gradual increase in pH to >10.5 led to an increase in the removal of $Al^{3+}$ and $Fe^{3+}$. The *RE* for $Al^{3+}$, $Fe^{3+}$, $Mn^{2+}$, $Pb^{2+}$, $Ni^{2+}$, $Zn^{2+}$, $Cr^{2+}$ and $Cu^{2+}$ were observed to be ≥99.9% whilst the *RE* for sulfate from real AMD was observed to be ≥40%. Furthermore, PHREEQC geochemical model predicted the removal of metals as hydroxides:

$$M^{n+} + nOH^- \rightarrow M(OH)_n \downarrow \qquad (2)$$

Residual sulfate could be removed using polishing technologies such as adsorption, membrane filtration, ion exchange and bio-(phyto)-remediation. The main quest will be to reclaim water that complies with the specified limits. In light of the optimisation study, it appears that 10 g/dm$^3$ is the optimum dosage of $Ca^{2+}$-rich MgO NPs for both metals and $SO_4^{2-}$ removal. Chemical species were predicted to be removed through different mechanisms such as adsorption, precipitation, complexation, co-precipitation, and co-adsorption specifically through the formation of gypsum, di-(tri)-metals sulfates, epsomite and oxyhydrosulfates.

## 3.2. TREATMENT OF REAL AMD UNDER OPTIMUM CONDITIONS

As shown in Table 1, the use of the $Ca^{2+}$-rich MgO NPs could provide a viable option for the effective management of AMD. In particular, $Ca^{2+}$-rich MgO NPs treatment largely reduced the levels of the contaminants contained in AMD, suggesting that it is possible to treat real and concentrated AMD. This hybrid process makes use of synergies between adsorption, ion exchange, and precipitation primarily due to the chemical components embedded in its matrices. pH of AMD was observed to increase from 2 to 10.9 (Table 1), indicating that the alkalinity released from the $Ca^{2+}$-rich MgO NPs matrices played an indispensable role in the attenuation of inorganic contaminants including sulfate. Nearly all $Pb^{2+}$, $Zn^{2+}$, $Al^{3+}$ and $Fe^{3+}$ content was removed, while the percentage removal for $Mn^{2+}$, $Cr^{2+}$, and $Ni^{2+}$ was >99.9%, while $Cu^{2+}$ attained 99.8%, and sulfate attained ≥ 40% (decrease from 15 000 to 9000 mg/dm$^3$). Lastly, an increase

of $Ca^{2+}$, $Mg^{2+}$, and *EC* levels was observed, and this could be attributed to dissolution of $Mg^{2+}$ and $Ca^{2+}$ from the matrices of the $Ca^{2+}$-rich MgO NPs.

Table 1

Contents and physicochemical properties
of the raw and $Ca^{2+}$-rich MgO NPs treated AMD

| Element | Real AMD | Treated AMD | *ER* |
|---|---|---|---|
| $SO_4^{2-}$, mg/dm³ | 15000 | 9000.0 | 40.0 |
| $Fe^{3+}$, mg/dm³ | 1800 | 0.1 | 100.0 |
| $Al^{3+}$, mg/dm³ | 500 | 0.1 | 100.0 |
| $Mn^{2+}$, mg/dm³ | 98 | 0.1 | 99.9 |
| $Cr^{2+}$, mg/dm³ | 0.09 | 0.0 | 99.9 |
| $Zn^{2+}$, mg/dm³ | 120 | 0.0 | 100.0 |
| $Cu^{2+}$, mg/dm³ | 0.59 | 0.0 | 99.8 |
| $Ni^{2+}$, mg/dm³ | 1.6 | 0.0 | 99.9 |
| $Pb^{2+}$, mg/dm³ | 0.2 | 0.0 | 100.0 |
| pH | 2 | 10.9 | – |
| *EC*, mS/cm | 1709 | 2100.0 | – |
| $Ca^{2+}$, mg/dm³ | 495 | 598.0 | – |
| $Mg^{2+}$, mg/dm³ | 622 | 3783.0 | – |

The presence of $Fe^{3+}$ and $SO_4^{2-}$ ions at elevated concentrations suggests that the mine water being treated in this study originates from the oxidation of pyrite [20]. Thenceforth, other inorganic contaminants denote the presence of other sulfide minerals, i.e., $Zn^{2+}$, $Cu^{2+}$, $Zn^{2+}$ and $Ni^{2+}$ associated with coal strata and those were possibly incorporated into coal matrices during their genesis process [21]. Increases in $Ca^{2+}$ concentration and *EC* level were expected but an increase in $Mg^{2+}$ content required applying another technology to meet standards for drinking water or any other defined use such as softening and reverse osmosis (RO).

### 3.3. SOLID MATERIALS CHARACTERISATION

As shown in Table 2, $Ca^{2+}$-rich MgO NPs and $Ca^{2+}$-rich MgO NPs-AMD resultant sludge (sludge) comprised $Mg^{2+}$, $Ca^{2+}$ and $Si^{+}$(Ca-enriched MgO). After contacting $Ca^{2+}$-rich MgO NPs with AMD solution, the resultant sludge comprised elements typical of AMD and $Ca^{2+}$-rich MgO NPs. Specifically, the resultant sludge comprised elevated levels of $Fe^{3+}$, $Mg^{2+}$, $Al^{3+}$, $Ca^{2+}$, $S^{2-}$, and $Si^{+}$. The detected elements are the major contaminants in AMD hence confirming that $Ca^{2+}$-rich MgO NPs act as a sink of major and trace contaminants from AMD which confirms the ICP-MS results as reported in the optimization studies. There was an insignificant shift in the level of trace elements. The reduction of $Mg^{2+}$ content in the sludge confirms what has been reported in the ICP results where the concentrations of $Mg^{2+}$ and $Ca^{2+}$ increased in the product water (Table 1).

Findings from this section further confirm what has been predicted by PHREEQC geochemical model that metals were removed as hydroxides, oxyhydroxides, oxy-hydrosulfates, carbonates, and metals sulfates including gypsum. The loss of ignition (LOI) was also observed to be high. This could be mainly traced back to the water, since this material is hydrated, and to a lesser extent to volatile compounds, organic matter, and carbonates.

Table 2

The chemical composition of $Ca^{2+}$-rich MgO NPs and $Ca^{2+}$-rich MgO NPs-AMD resultant sludge obtained by the XRF technique [wt. %]

| Component | Standard | | Characterisation | |
|---|---|---|---|---|
| | BHVO-1 STD | BHVO-1 analysed | Ca-rich MgO NPs | Sludge |
| $SiO_2$ | 49.94 | 48.17 | 1.81 | 1.44 |
| $Al_2O_3$ | 13.8 | 17.33 | 0.29 | 3.13 |
| MgO | 7.23 | 5.96 | 81.84 | 40.51 |
| $Na_2O$ | 2.26 | 2.94 | <0,01 | <0,01 |
| $P_2O_5$ | 0.273 | 0.31 | 0.04 | 0.03 |
| $Fe_2O_3$ | 12.23 | 10.98 | 0.18 | 15.89 |
| $K_2O$ | 0.52 | 0.57 | <0,01 | 0.01 |
| CaO | 11.4 | 10.82 | 6.08 | 3.39 |
| $TiO_2$ | 2.71 | 2.50 | <0.01 | <0.01 |
| $V_2O_5$ | 0.0566 | 0.06 | <0.01 | <0.01 |
| $Cr_2O_3$ | 0.0422 | 0.04 | <0,01 | <0.01 |
| MnO | 0.168 | 0.17 | 0.01 | 0.32 |
| NiO | 0.0154 | 0.01 | <0,01 | <0.01 |
| CuO | 0.017 | 0.02 | <0,01 | <0.01 |
| $ZrO_2$ | 0.0242 | 0.02 | 0.02 | <0.01 |
| $SO_3$ | – | 0.01 | 0.51 | 2.54 |
| $Nb_2O_5$ | – | – | 0.02 | 0.01 |
| $Co_3O_4$ | – | 0.02 | <0.01 | 0.02 |
| ZnO | – | – | <0.01 | 0.03 |
| SrO | – | 0.04 | 0.09 | 0.03 |
| $Y_2O_3$ | – | – | <0.01 | 0.01 |
| LOI | – | – | 9.06 | 32.59 |

The HR FE-SEM images of $Ca^{2+}$-rich MgO NPs and Ca-rich MgO NPs-AMD resultant sludge are shown in Fig. 3. The $Ca^{2+}$-rich MgO NPs were observed to comprise heterogeneous mixtures of connected octagonal nano-sheets (Fig. 3a) similar in different magnifications and this confirms literature reports [1, 12, 14]. $Ca^{2+}$-rich MgO NPs--AMD resultant sludge was observed to comprise leafy-like structures and the nanosheets were decomposed. The results confirm the microstructural transformation of the material; new mineral phases deposit to the sludge from AMD (Fig. 3b). This

further confirms the removal and dissolution of contaminants from AMD by means of $Ca^{2+}$-rich MgO NPs.
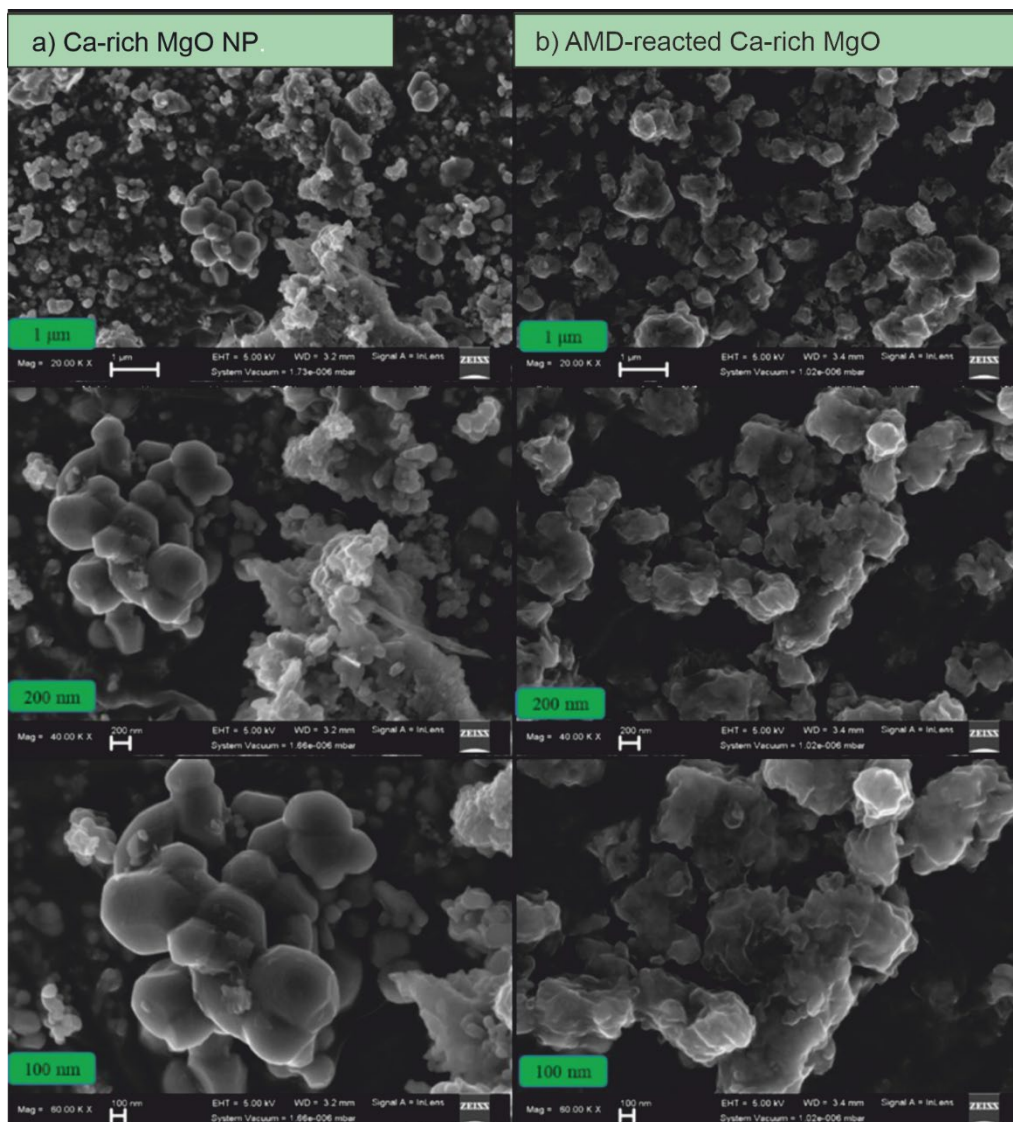


Fig. 3. HR FE-SEM images of $Ca^{2+}$-rich MgO NPs (a)
and $Ca^{2+}$-rich MgO NPs-AMD (b) resultant sludge

To further confirm the XRF and the SEM/EDS results regarding the elemental compositions of the examined solid samples, elemental distribution mapping was also carried out using the FE-SEM instrument's EDS capabilities. Results are shown in Fig. 4.
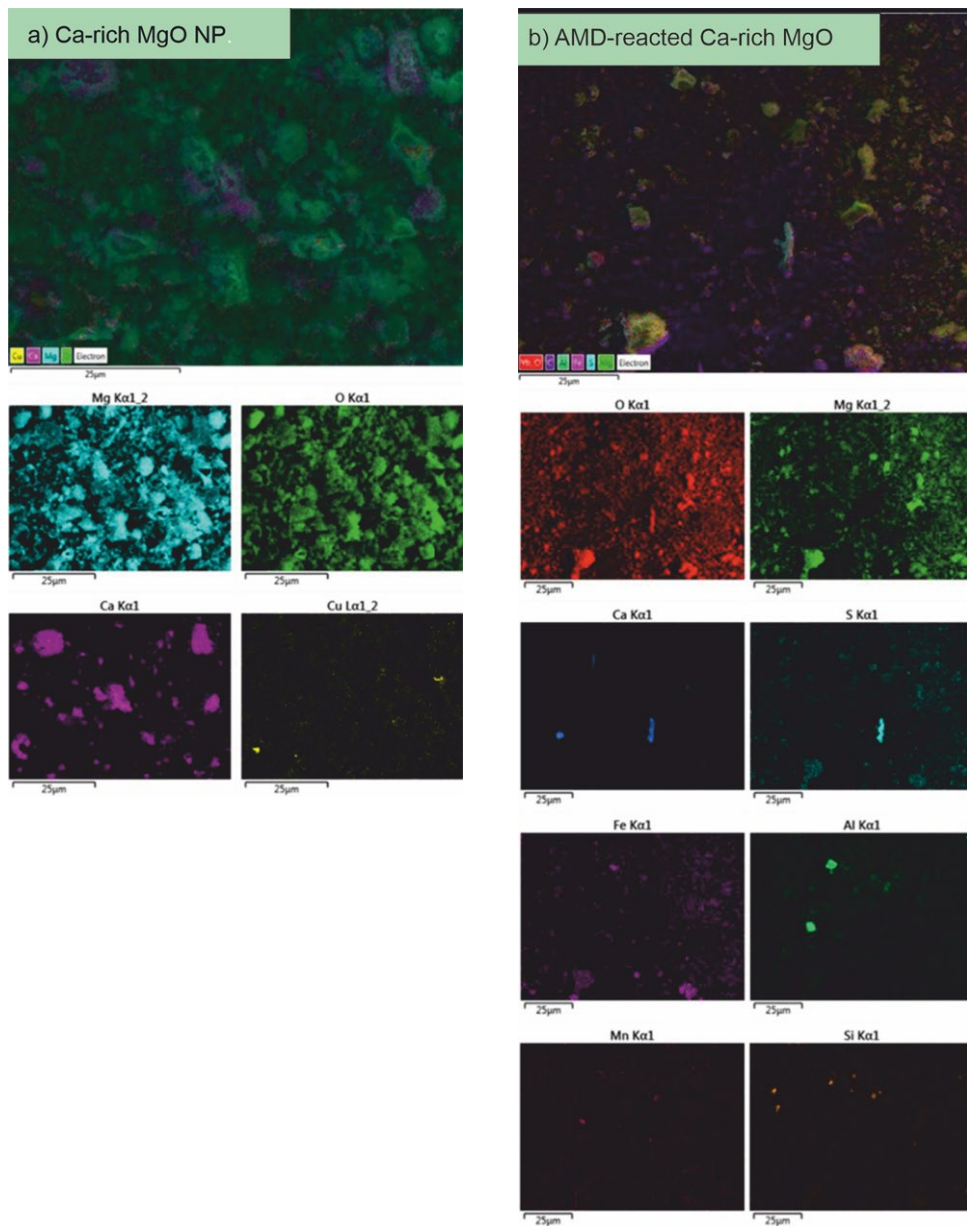
Fig 4. The EDS/SEM images and elemental maps of $Ca^{2+}$-rich MgO NPs (a)
and $Ca^{2+}$-rich MgO NPs-AMD (b) resultant sludge

The $Ca^{2+}$-rich MgO NPs comprised $Mg^{2+}$, $O^{2-}$, and $Ca^{2+}$ ions as dominant elements along with very low levels of $Cu^{2+}$ (Fig. 4a). The presence of $Cu^{2+}$ is due to the coating

material that was used during the analysis of the samples. The elements were fairly distributed across the surface, hence confirming their predominance, confirming the nature of the material being used in this study. The obtained results correspond to those obtained by the XRF and EDS. The resultant sludge (Fig. 4b) comprised $O^{2-}$, $Fe^{3+}$, $S^{2-}$, $Ca^{2+}$, and $Mg^{2+}$ as major elements. Traces of $Mn^{2+}$, $Si^+$, and $Al^{3+}$ were also observed. The obtained results confirm predictions by the PHREEQC geochemical model where sulfate was removed as gypsum. This could be confirmed by the presence of notable levels of $Ca^{2+}$, $S^{2-}$ and $O^{2-}$. Similar results have been reported in the literature [1]. $Al^{3+}$, $Fe^{3+}$, and $O^{2-}$ ions were detected, and this could imply the formation of Al and Fe hydroxide, however, the PHREEQC tests showed that these chemicals are removed as oxy-(hydro)-sulfates, metal-(hydro)-sulfates, and hydroxides, amongst others. This could be explained by the presence of $O^{2-}$, $Fe^{3+}$, and $Al^{3+}$ ions. $Mg^{2+}$ ions were also found, probably released from $Ca^{2+}$-rich MgO NPs matrices. The obtained results confirm the ICP-MS/OES results on the raw and product water quality, demonstrating the fate of chemical components after the treatment of AMD with $Ca^{2+}$-rich MgO NPs.
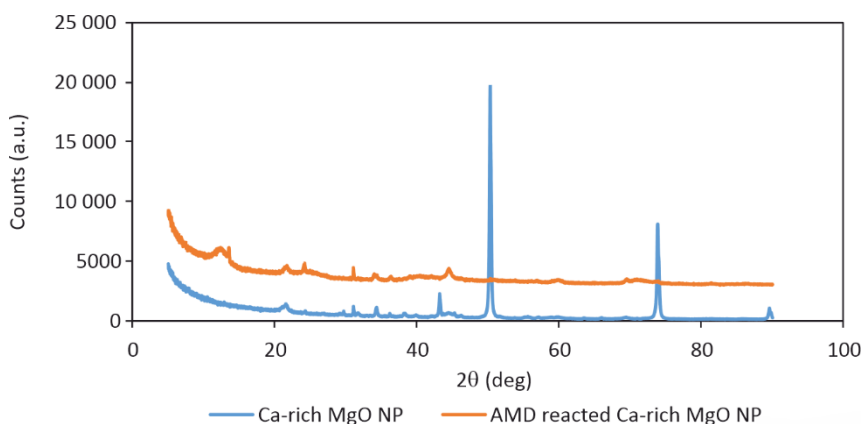


Fig. 5. Mineralogical composition of the $Ca^{2+}$-rich MgO NPs
and $Ca^{2+}$-rich-MgO nanocomposite-AMD resultant sludge

The mineralogical compositions and crystal phases of the examined solid samples identified using the XRD method are shown in Fig. 5. The crystal mineral phases of $Ca^{2+}$-rich MgO NPs and $Ca^{2+}$-rich MgO NPs-AMD resultant sludge were identified. $Ca^{2+}$-rich MgO NPs comprised periclase, brucite, quartz, calcite, anhydrite, and magnesite. The presence of base metals and Si species would significantly contribute to the increase in alkalinity, and this will aid in the removal of metals through precipitation, co-precipitation and adsorption as predicted by PHREEQC geochemical model. Specifically, the silicate would react with acidity in AMD using ion exchange as a mechanism, hence increasing the pH of the product water (Eqs. (3)–(7)) [22].

$$\equiv SiOH \leftrightarrow SiO + H^+ \tag{3}$$

$$\equiv SiOH + Ca^{2+} \leftrightarrow =SiOCa + H^+ \tag{4}$$

$$= SiOCa + M^{2+} + 2HOH \rightarrow =SiOM + Ca^{2+} + 2OH^- \tag{5}$$

$$\equiv SiOH + Mg \leftrightarrow =SiOMg + H^+ \tag{6}$$

$$\equiv SiOMg + M^{2+} + 2HOH \rightarrow +SiOM + Mg^{2+} + 2OH^- \tag{7}$$
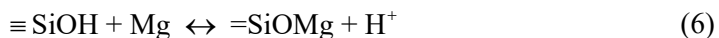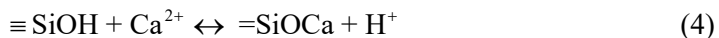
The $Ca^{2+}$-rich MgO NPs-AMD resultant sludge comprised gypsum, quartz, brucite, epidote, sjoegrenite, and nordstrandite as well as amorphous phases. The reaction of the Ca-rich MgO NPs and AMD remains in agreement with the XRD, EDS mapping, XRF, and PHREEQC geochemical modelling results and this could further be explained by the following equations [23].

$$CaO + H_2O \rightarrow Ca(OH)_2 \tag{8}$$

$$MgSO_4 + Ca(OH)_2 \rightarrow Mg(OH)_2 + CaSO_4 \tag{9}$$
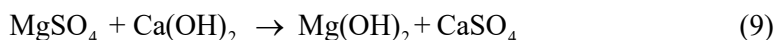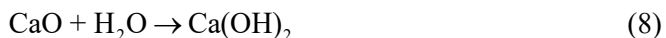
The presence of new phases demonstrates the decomposition of $Ca^{2+}$-rich MgO NPs and the formation of new mineral phases. The disappearance of periclase, calcite and magnesite confirms the alkalinity in the product waste:

$$Al(H_2O)_3(OH)_3 + SO_4^{2-} \rightarrow Al(H_2O)_3OHSO_4 + 2OH^- \tag{10}$$

$$Fe(H_2O)_3(OH)_3 + SO_4^{2-} \rightarrow Fe(H_2O)_3OHSO_4 + 2OH^- \tag{11}$$
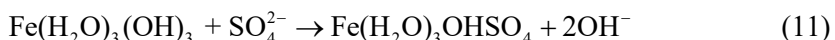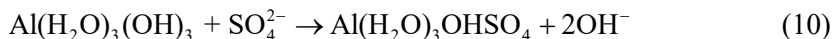
The results from this study confirm what has been reported in ICP-MS/OES, SEM--EDS, and PHREEQC geochemical modelling. This denotes the validity of the results and simulations thereto.

Finally, the elemental composition and FTIR spectra of the solid samples were also identified, along with their functional groups and wavenumbers. The results for $Ca^{2+}$--rich MgO NPs and $Ca^{2+}$-rich MgO NPs-AMD resultant sludge are shown in Fig. 6 and Table 3.

As shown in Fig. 6a, the used $Ca^{2+}$-rich MgO NPs comprised $Mg^{2+}$, $O^{2-}$ and $Ca^{2+}$ as the main components. This confirms that the material is magnesium oxide that is rich in $Ca^{2+}$ hence the name $Ca^{2+}$-rich MgO NP. The results confirm the XRF results. However, after contacting AMD (Fig. 6b), the levels of $O^{2-}$, $Fe^{3+}$, $S^{2-}$, $Al^{3+}$, $Si^+$, $Mn^{2+}$, and $K^+$ were observed to have increased/introduced hence confirming the formation of Fe hydroxide, metals-oxy-hydrosulfate, and gypsum as predicted by the PHREEQC geochemical model.
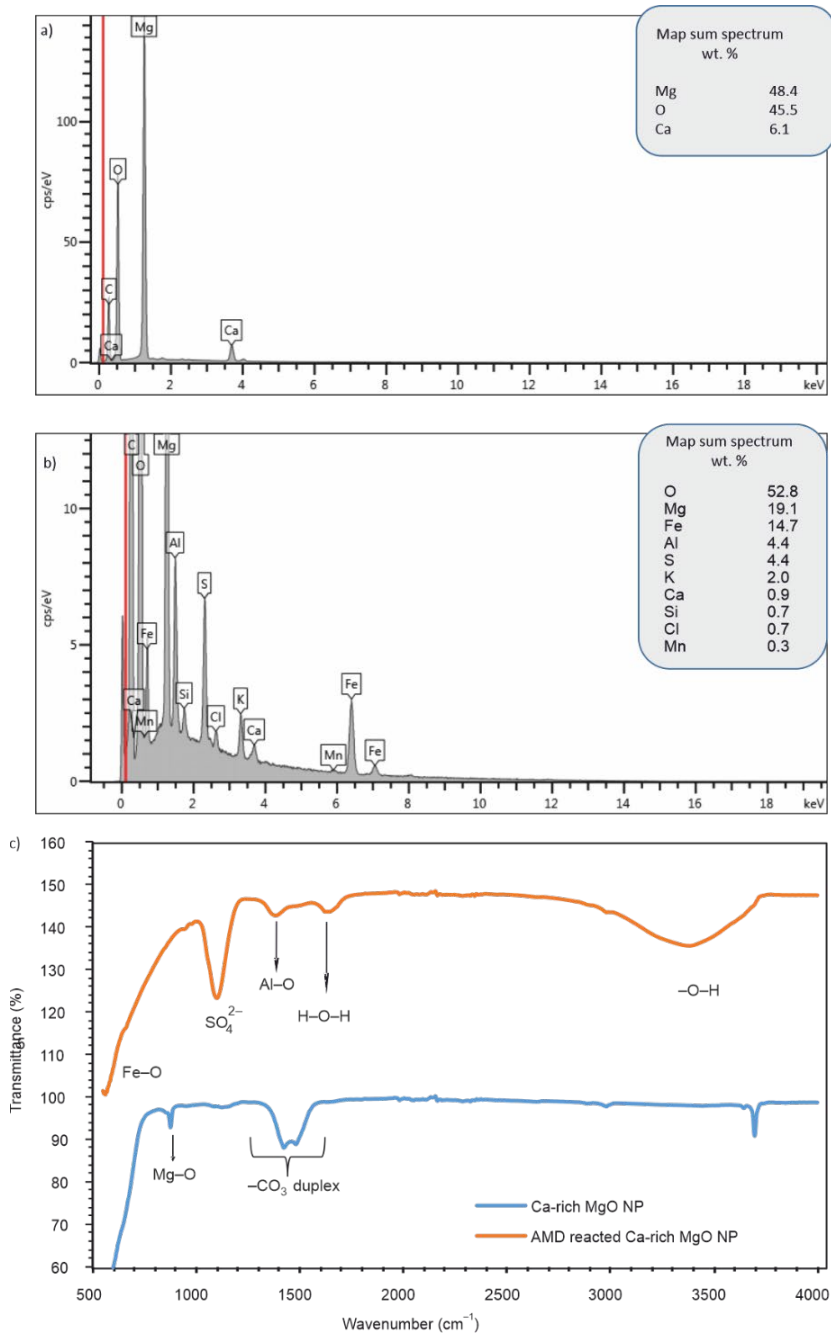
Fig. 6. The elemental composition and FTIR spectra of $Ca^{2+}$-rich MgO nanocomposite (a),
$Ca^{2+}$-rich MgO nanocomposite-AMD resultant sludge (b), and their transmittance spectra (c)

Mg$^{2+}$ and Ca$^{2+}$ contents were observed to have decreased hence denoting the dissolution of these chemical species from the matrices and inter-layers of Ca$^{2+}$-rich MgO NPs. This could be confirmed by their increase in the product water (as reported by ICP-MS/OES) and elevated electrical conductivity of the treated water (Table 1). Findings obtained in this study further confirm that Ca$^{2+}$-rich MgO NPs could scavenge contaminants from AMD , and this could be confirmed by their fate as confirmed by multiple tools such as the ICP-MS, XRF, and SEM-EDS including PHREEQC geochemical model.

Table 3

FTIR results for Ca$^{2+}$-rich MgO NPs and Ca$^{2+}$-rich MgO NPs-AMD resultant sludge

| Material | Chemical species | Wavenumber [cm$^{-1}$] | Reference |
|---|---|---|---|
| MgO NPs | MgO | 900 | [24] |
| | CO$_3$ | 1400–1600 | |
| | H–O–H | 3700 | |
| MgO NPs-AMD sludge | Al–O–Si | 800–900 | [16, 25, 26] |
| | Fe–O | 550–600 | |
| | H–O–H | 1600, 3300 | |
| | Al–O | 1400 | |
| | SO$_4$ | 1100 | |

As shown in Fig. 6c and Table 3, the obtained FTIR results confirm the XRF, XRD, EDS/SEM and PHREEQC geochemical modelling results. In a nutshell, it appears that the use of the Ca$^{2+}$-rich-MgO NPs can act as an innovative avenue for the treatment of AMD. Therefore, with this hybrid co-treatment method, the effective management of AMD from coal mining can be achieved, while water could also be reclaimed using polishing technologies. This is of particular importance for South Africa and other countries and areas that are affected by water scarcity and notorious mining activities. In particular, raw Ca$^{2+}$-rich MgO NPs comprised Mg-O, CO$_3$, and OH groups. This shows that the material is magnesium based and it contains water. The carbonate fraction confirms its origin. However, after the interaction of Ca$^{2+}$-rich MgO NPs with AMD, species originating from AMD such as S$^{2-}$, Al$^{3+}$, Fe$^{3+}$, and OH$^-$ were observed in the sludge and they include.

## 4. ESTIMATION OF THE SATURATION INDICES (SIS)

The results for the estimation of mineral precipitation during the treatment of AMD with Ca$^{2+}$-rich MgO NPs are presented in Table 4. Estimated saturation indices (*SI*) for mineral precipitation predictions are shown in Table 5.

T a b l e   4

Estimation of the speciation of the chemicals in real acid mine drainage (AMD)

| Element | Speciation | Element | Speciation | Element | Speciation |
|---------|------------|---------|------------|---------|------------|
| Al | $Al^{3+}$ | Fe | $Fe^{3+}$ | Pb | $Pb^{2+}$ |
|  | $Al(SO_4)^{2-}$ |  | $Fe(SO_4)^{2-}$ |  | $PbSO_4$ |
|  | $Al(OH)_3$ |  | $Fe(OH)_3$ |  | $PbCO_3$ |
| Ca | $Ca^{2+}$ | Mg | $Mg^{2+}$ | S | $SO_4^{2-}$ |
|  | $CaSO_4$ |  | $MgSO_4$ |  | $MgSO_4$ |
|  | $CaCO_3$ |  | $MgCO_3$ |  | $CaSO_4$ |
| Cr | $Cr^{3+}$ | Mn | $Mn^{2+}$ |  | $MnSO_4$ |
|  | $Cr(OH)_3$ |  | $Mn^{3+}$ |  | $CuSO_4$ |
|  | $Cr(OH)^{2+}$ |  | $MnCO_3$ |  | $PbSO_4$ |
| Cu | $Cu^{2+}$ | Ni | $Ni^{2+}$ |  | $NiSO_4$ |
|  | $CuSO_4$ |  | $NiSO_4$ | Zn | $Zn^{2+}$ |
|  | $Cu(OH)_2$ |  | $NiCO_3$ |  | $ZnSO_4$ |
|  | $CuCO_3$ |  |  |  | $ZnCO_3$ |

T a b l e   5

Estimated saturation indices (*SI*) for mineral precipitation predictions

| Mineral | Chemical formula | *SI* | Mineral | Chemical formula | *SI* |
|---------|------------------|------|---------|------------------|------|
| Alunite | $KAl(SO_4)_2(OH)_6$ | 6.92 | Goethite | $FeOOH$ | 6.18 |
| Epsomite | $MgSO_4$ | 0.93 | Gypsum | $CaSO_4 \cdot 2H_2O$ | 3.89 |
| Anglesite | $PbSO_4$ | 4.81 | Hematite | $Fe_2O_3$ | 16.85 |
| Anhydrite | $CaSO_4$ | 3.90 | Hausmannite | $Mn_3O_4$ | 1.6 |
| Antlerite | $CaCO_3$ | 11.06 | Jarosite-Na | $NaFe_3(SO_4)_2(OH)_6$ | 16.28 |
| Aragonite | $Cu_3(OH)_2(CO_3)_2$ | 5.62 | Manganite | $MnOOH$ | 1.6 |
| Azurite | $Cu_3(OH)_2(CO_3)_2$ | 19.48 | $Ni(OH)_2$ | $Ni(OH)_2$ | 1.41 |
| Basaluminite | $Al_4(OH)10SO_4$ | 1.16 | $Pb(OH)_2$ | $Pb(OH)_2$ | 4.04 |
| Bixbyite | $Mn_2O_3$ | 4.01 | $Pb_4(OH)6SO_4$ | $Pb_4(OH)6SO_4$ | 8.47 |
| Boehmite | $AlOOH$ | 2.51 | Pyrochroite | $Mn(OH)_2$ | 0.63 |
| Brochantite | $Cu_4(OH)6SO_4$ | 16.91 | Rodochrosite | $MnCO_3$ | 8.97 |
| Brucite | $Mg(OH)_2$ | 1.80 | $Zn(OH)_2$ | $Zn(OH)_2$ | 2.38 |
| Calcite | $CaCO_3$ | 5.76 | Crocoite | $PbCrO_4$ | 0.95 |
| Cerrusite | $PbCO_3$ | 7.46 | Chromite | $FeCr_2O_4$ | 17.30 |
| $Cu(OH)_2$ | $Cu(OH)_2$ | 4.26 | $CuCr_2O_4$ | $CuCr_2O_4$ | 10.09 |
| $CuCO_3$ | $CuCO_3$ | 4.47 | $Fe(OH)_3$ | $Fe(OH)_3$ | 6.67 |
| Cupricferrite | $CuFe_2O_4$ | 17.97 | Hydrocerrusite | $Pb(OH)_2:2PbCO_3$ | 18.04 |
| Diaspore | $AlOOH$ | 4.21 | Hydromagnesite | $Mg_5(CO_3)_4(OH)_2:4H_2O$ | 28.81 |
| Dolomite | $CaMg(CO_3)_2$ | 14.41 | Magnetite | $Fe_3O_4$ | 14.35 |
| $Fe(OH)_3$ | $Fe(OH)_3$ | 1.36 | Malachite | $Cu_2(OH)_2CO_3$ | 12.58 |
| Gibbsite | $Al(OH)_3$ | 2.69 | Smithsonite | $ZnCO_3$ | 6.14 |

As shown in Table 5, various chemicals precipitated from the mixture of $Ca^{2+}$-rich MgO NPs with AMD. The carbonates were observed to be present, and this could also be linked to atmospheric interactions during the treatment. A variety of minerals was observed to be formed as predicted by PHREEQC geochemical model, Thenceforth, the obtained mineral is congruent to what has been reported in FTIR, XRD, XRF, and HR--FIB-SEM-EDS including amorphous phases that could not be detected using XRD since its capability is limited to crystalline phases. The obtained results further confirm what has been reported in the literature [8, 14].

## 5. CONCLUSIONS

This study proved the effectiveness of $Ca^{2+}$-rich MgO NPs in treating real acid mine drainage (AMD) from coal mining processes. The obtained results were underpinned using state-of-the-art analytical techniques and instruments, such as FTIR, HR-FIB /SEM, EDS, XRF, and XRD. The pH REDOX equilibrium (PHREEQC) was employed in C language to complement experimental results. Optimum conditions were observed to be 45 min of mixing time, $\geq 10$ g/dm$^3$ of feedstock dosage, i.e., $Ca^{2+}$-rich MgO NPs at ambient temperature and pH. The metal content ($Fe^{3+}$, $Mn^{2+}$, $Cr^{2+}$, $Cu^{2+}$, $Ni^{2+}$, $Pb^{2+}$, $Al^{3+}$, and $Zn^{2+}$) embedded in AMD matrices was practically depleted (>99% removal) and sulfates greatly reduced ($\geq 40\%$). PHREEQC predicted metals to exist as mono-, di-, and tri-valent, including the variety of chemical complexes and carbonates, and they precipitated as metals hydroxides, (oxy)-hydroxides, carbonates, and (oxy)-hydro-sulfates. This treatment approach holds great promise for the sustainable management of AMD effluents from coal mining activities and can provide a simple and effective solution for its management. Softening and filtration technologies will need to be coupled to this process to further enhance the reclamation of drinking and to explore the possible recovery of valuable minerals from the generated sludge.

### REFERENCES

[1] MASINDI V., CHATZISYMEON E., KORTIDIS I., FOTEINIS S., *Assessing the sustainability of acid mine drainage (AMD) treatment in South Africa*, Sci. Total Environ., 2018, 635, 793–802. DOI: 10.1016 /j.scitotenv.2018.04.108.

[2] MASINDI V., FOTEINIS S., CHATZISYMEON E., *Co-treatment of acid mine drainage and municipal wastewater effluents: Emphasis on the fate and partitioning of chemical contaminants*, J. Hazard. Mater., 2022, 421, 126677. DOI: 10.1016/j.jhazmat.2021.126677.

[3] BAKER B.J., BAN J.F., *Microbial communities in acid mine drainage*, FEMS Microbiol. Ecol., 2003, 44, 139–152. DOI: 10.1016/S0168-6496(03)00028-X.

[4] HOGSDEN K.L., HARDING J.S., *Consequences of acid mine drainage for the structure and function of benthic stream communities. A review*, Freshwater Sci., 2012, 31 (1), 108–120, DOI: 10.1899/11-091.1.

[5] KEFENI K.K., MSAGATI T.M., MAMBA B.B., *Synthesis and characterization of magnetic nanoparticles and study their removal capacity of metals from acid mine drainage*, Chem. Eng. J., 2015, 276, 222–231. DOI: 10.1016/j.cej.2015.04.066.

[6] IGHALO J.O., KURNIAWAN S.B.,, IWUOZOR K.O., ANIAGOR O.C., AJALA O.J., OBA S.N., IWUCHUKWU F.U., AHMADI S., IGWEGBE C.A., *A review of treatment technologies for the mitigation of the toxic environmental effects of acid mine drainage (AMD)*, Proc. Saf. Environ. Prot., 2022, 157, 37–58, DOI: 10.1016/j.psep.2021.11.008.

[7] SHABALALA A.N., EKOLU S.O., *Quality of water recovered by treating acid mine drainage using pervious concrete adsorbent*, Water SA, 2019, 45 (4), 638–647. DOI: 10.17159/wsa/2019.v45.i4.7545.

[8] MASINDI V., FOSSO-KANKEU E., MAMAKOA E., NKAMBULE T.T.I., MAMBA B.B., NAUSHAD M., PANDEY S., *Emerging remediation potentiality of struvite developed from municipal wastewater for the treatment of acid mine drainage*, Environ. Res., 2021, 210, 112944. DOI: 10.1016/j.envres.2022.112944.

[9] PARK I., TABELIN C.B., JEON S., LI X., SENO K., ITO M., HIROYOSHI N., *A review of recent strategies for acid mine drainage prevention and mine tailings recycling*, Chemosphere, 2019, 219, 588–606. DOI: 10.1016/j.chemosphere.2018.11.053.

[10] MASINDI V., FOTEINIS S., *Recovery of phosphate from real municipal wastewater and its application for the production of phosphoric acid*, J. Environ. Chem. Eng., 2021, 9 (6), 106625. DOI: 10.1016/j.jece.2021.106625.

[11] NLEYA Y., SIMATE G.S., NDLOVU S., S*ustainability assessment of the recovery and utilisation of acid from acid mine drainage*, J. Clean. Prod., 2016, 113, 17–27. DOI: 10.1016/j.jclepro.2015.11.005.

[12] AKINWEKOMI V., MAREE J.P., MASINDI V., ZVINOWANDA C., OSMAN M.S., FOTEINIS S., *Beneficiation of acid mine drainage (AMD): A viable option for the synthesis of goethite, hematite, magnetite, and gypsum. Gearing towards a circular economy concept*, Miner. Eng., 2020, 148, 106204. DOI: 10.1016/j.mineng.2020.106204.

[13] AKINWEKOMI V., MAREE J.P., ZVINOWANDA C., MASINDI V., *Synthesis of magnetite from iron-rich mine water using sodium carbonate*, J. Environ. Chem. Eng., 2017, 5 (3), 2699–2707. DOI: 10.1016/j.jece.2017.05.025.

[14] MASINDI V., FOTEINIS S., CHATZISYMEON E., *Co-treatment of acid mine drainage and municipal wastewater effluents: Emphasis on the fate and partitioning of chemical contaminants*, J. Hazard. Mater., 2022, 421, 126677. DOI: 10.1016/j.jhazmat.2021.126677.

[15] BOLOGO V., MAREE J.P., CARLSSON F., *Application of magnesium hydroxide and barium hydroxide for the removal of metals and sulfate from mine water*, Water SA, 2012, 38 (1), 23–28. DOI: 10.4314 /wsa.v38i1.4.

[16] NGUEGANG B., MASINDI V., ALFRED T., MAKUDALI M., *Effective treatment of acid mine drainage using a combination of MgO nanoparticles and a series of constructed wetlands planted with Vetiveria zizanioides. A hybrid and stepwise approach*, J. Environ. Manage., 2022, 310, 114751. DOI: 10.1016/j.jenvman.2022.114751.

[17] MASINDI V., *Integrated treatment of acid mine drainage using cryptocrystalline magnesite and barium chloride*, Water Pract. Technol., 2017, 12 (3), 727–736. DOI: 10.2166/wpt.2017.074.

[18] MASINDI V., GITARI W.M., *Simultaneous removal of metal species from acidic aqueous solutions using cryptocrystalline magnesite/bentonite clay composite: An experimental and modelling approach*, J. Clean. Prod., 2016, 112, 1077–1085. DOI: 10.1016/j.jclepro.2015.07.128.

[19] Masindi V., Akinwekomi V., Maree J.P., Muedi K.L., *Comparison of mine water neutralisation efficiencies of different alkaline generating agents*, J. Environ. Chem. Eng., 2017, 5 (4), 3903–3913. DOI: 10.1016/j.jece.2017.07.062.

[20] Madzivire G., Maleka P.P., Vadapalli V.R.K., Gitari W.M., Lindsay R., Petrik L.F., *Fate of the naturally occurring radioactive materials during treatment of acid mine drainage with coal fly ash and aluminium hydroxide*, J. Environ. Manage., 2014, 133, 12–17. DOI: 10.1016/j.jenvman.2013.11.041.

[21] Simate G.S., Ndlovu S., *Acid mine drainage. Challenges and opportunities*, J. Environ. Chem. Eng., 2014, 2 (3), 1785–1803. DOI: 10.1016/j.jece.2014.07.021.

[22] Vhahangwele M., Mugera G.W., *The potential of ball-milled South African bentonite clay for attenuation of heavy metals from acidic wastewaters: Simultaneous sorption of $Co^{2+}$, $Cu^{2+}$, $Ni^{2+}$, $Pb^{2+}$, and $Zn^{2+}$ ions*, J. Environ. Chem. Eng., 2015, 3 (4), 2416–2425. DOI: 10.1016/j.jece.2015.08.016.

[23] Masindi V., Gitari M.W., Tutu H., Debeer M., *Removal of boron from aqueous solution using magnesite and bentonite clay composite*, Desalin. Water Treat., 2016, 57 (19), 8754–8764. DOI: 10.1080/19443994.2015.1025849.

[24] Magagane N., Masindi V., Mercy M., Brendon M., Lilith K., *Facile thermal activation of non-reactive cryptocrystalline magnesite and its application on the treatment of acid mine drainage*, J. Environ. Manage., 2018, 236, 499–509. DOI: 10.1016/j.jenvman.2019.02.030.

[25] Lin M., Liu Y., Lei S., Ye Z., Pei Z., Li B., *Applied clay science high-efficiency extraction of Al from coal-series kaolinite and its kinetics by calcination and pressure acid leaching*, 2018, 161, 215–224. DOI: 10.1016/j.clay.2018.04.031.

[26] Nguegang B., Masindi V., Msagati T.A.M., *The treatment of acid mine drainage using vertically flowing wetland. Insights into the fate of chemical species*, Minerals, 2021, 11 (5), 477. DOI: 10.3390/min11050477.